

■ Radical Cations

Formation of the Charge-Localized Dimer Radical Cation of 2-Ethyl-9,10-dimethoxyanthracene in Solution Phase

Jungkweon Choi^{+, [a, b]} Doo-Sik Ahn^{+, [a, b]} Mamoru Fujitsuka,^[c] Sachiko Tojo,^[c] Hyotcherl Ihee,^{*, [a, b]} and Tetsuro Majima^{*, [c]}

Abstract: Although dimer radical ions of aromatic molecules in the liquid-solution phase have been intensely studied, the understanding of charge-localized dimers, in which the extra charge is localized in a single monomer unit instead of being shared between two monomer units, is still elusive. In this study, the formation of a charge-localized dimer radical cation of 2-ethyl-9,10-dimethoxyanthracene (DMA), (DMA)₂^{•+} is investigated by transient absorption (TA) and time-resolved resonance Raman (TR³) spectroscopic methods combined with a pulse radiolysis technique. Visible- and near-IR TA signals in highly concentrated DMA solutions supported the formation of non-covalent (DMA)₂^{•+} by association of DMA and DMA^{•+}. TR³ spectra obtained from 30 ns to 300 μs time delays showed that the major bands are quite similar to those of DMA except for small transient bands, even at

30 ns time delay, suggesting that the positive charge of non-covalent (DMA)₂^{•+} is localized in a single monomer unit. From DFT calculations for (DMA)₂^{•+}, our TR³ spectra showed the best agreement with the calculated Raman spectrum of charge-localized edge-to-face T-shaped (DMA)₂^{•+}, termed DT^{•+}, although the charge-delocalized asymmetric π-stacked face-to-face (DMA)₂^{•+}, termed DF3^{•+}, is the most stable structure of (DMA)₂^{•+} according to the energetics from DFT calculations. The calculated potential energy curves for the association between DMA^{•+} and DMA showed that DT^{•+} is likely to be efficiently formed and contribute significantly to the TR³ spectra as a result of the permanent charge-induced Coulombic interactions and a dynamic equilibrium between charge localized and delocalized structures.

Introduction

Positive and negative charges of radical ions, which are generated by one-electron oxidation and reduction of a molecule, respectively, can be either localized or delocalized in a molecule. Such charge localization and delocalization in a molecule is fundamental for understanding the stabilization and transportation of charges and is related to the reactivity of the molecule.^[1,2] In this regard, aromatic hydrocarbons that can easily undergo one-electron oxidation/reduction have been widely

recognized as good model systems for studying charge localization/delocalization in their radical ions as well as charge stabilization through charge-resonance dimerization.^[3–16]

Experimentally, charge delocalization over multiple units has been identified with characteristic absorption bands in the near-IR region due to the spatial overlap of π-orbitals.^[4,6,14,16] Such key spectroscopic signatures have been used for studying the kinetics of formation, transportation, and annihilation of charge carriers, such as radical ions in organic and biomolecular systems. By using the characteristic absorption bands in the near-IR region, previous studies on a variety of aromatic ring systems showed that charge delocalization through the spatial overlap of π-orbitals between identical aromatic rings induces dimerization of radical anions as well as radical cations.^[6,7,16–18] Dimerization of radical ions has also been observed in multiple aromatic systems with covalent linkers^[6] as well as in heterogeneous ring systems, such as pyrene-naphthalene radical cations.^[18] In particular, Majima and co-workers reported that both radical cations and anions of [3_n] cyclophane generated by pulse radiolysis are stabilized by the charge-resonance interactions between benzene rings and that the positive charge of multilayered cyclophanes is also stabilized by the aromatic charge-resonance interactions among π-stacked benzene ring moieties.^[6,9,17] In addition, the folding kinetics of a DNA strand were measured by monitoring the charge resonance (charge delocalization) band on the micro- to millisecond time scale.^[10–12]

[a] Dr. J. Choi,⁺ Dr. D.-S. Ahn,⁺ Prof. Dr. H. Ihee
Center for Nanomaterials and Chemical Reactions
Institute for Basic Science (IBS)
Daejeon 305-701 (Korea)
E-mail: hyotcherl.ihee@kaist.ac.kr

[b] Dr. J. Choi,⁺ Dr. D.-S. Ahn,⁺ Prof. Dr. H. Ihee
Department of Chemistry and KI of the BioCentury
Korea Advanced Institute of Science and Technology (KAIST)
Daejeon 305-701 (Korea)

[c] Dr. M. Fujitsuka, S. Tojo, Prof. Dr. T. Majima
The Institute of Scientific and Industrial Research (SANKEN)
Osaka University
Mihogaoka 8-1, Ibaraki, Osaka 567-0047 (Japan)
E-mail: majima@sanken.osaka-u.ac.jp

[*] These authors contributed equally to this work.

Supporting information and the ORCID identification number(s) for the author(s) of this article can be found under:
<https://doi.org/10.1002/chem.201900175>.

Spectroscopic evidence for the existence of charge-localized states, in which the extra charge is localized in a single unit instead of being spread in multiple units, in symmetric molecular systems also has been presented.^[19–25] In particular, the stable charge-localized state has been studied in anionic mixed-valence compounds, which contain two identical redox centers.^[19–24] For example, Hoekstra et al. have suggested the coexistence of charge-localized and -delocalized 4,4'-dinitrotolane radical anions on the basis of resonance Raman spectra and the equilibrium between the two states can be shifted by changing the solvent polarity.^[21,22] Furthermore, Jiang et al. have shown that, in anionic bay-linked perylene bisimides, the proportions of charge-localized and -delocalized states in the entire unit can be changed by applying different external electric potentials.^[24] In another study, Majima et al. have described the charge-localized σ -dimerization of radical anions of aromatic acetylenes.^[25]

Several studies on the structure of dimeric radical ions have focused on the existence of charge-localized dimer radical ions induced by conformational flexibility in solution.^[7,16,25–29] For example, the major structure of the benzene dimer radical cation has long been debated.^[7,30–35] Although a slipped face-to-face configuration has been accepted as the dominant species characterized by a charge resonance band in solution and gas phases, other tilted face-to-face dimers, and T-shaped dimer radical cations with charge localization have also been discussed as possible conformations.^[30,31] The charge distribution in the dimer radical cation conformers and the formation of covalent bond-linked dimers in gas phase have been discussed in other aromatic systems as well.^[36–38] Despite such extensive studies, the formation of dimer radical cations and the nature of charge localization/delocalization are not fully understood, especially for molecular units that are more complicated than simple benzene-type units.

To shed light on this topic, we chose 2-ethyl-9,10-dimethoxyanthracene (DMA) as our model target system. Anthracene and its derivatives have been widely investigated as prototypical molecular systems for dimerization initiated by photoexcitation and one-electron oxidation.^[28,39] Recently, Chen et al. have shown that radical cations of 2-ethyl-9,10-dimethoxyanthracene ($\text{DMA}^{\bullet+}$) exist dominantly as monomers in solution, whereas dimerization of the radical cations occurs upon crystallization.^[26] In the present study, we conducted transient absorption (TA) and time-resolved resonance Raman (TR^3) spectroscopic measurements using pulse radiolysis of DMA dissolved in 1,2-dichloroethane (DCE). Pulse radiolysis, which can easily and selectively generate radical ions, is highly effective in investigating the changes induced by additional charges in the solution.^[5,7,16,23–28] The results obtained from the TA and TR^3 experiments and density functional theory (DFT) calculations indicate the charge-localized DMA dimer radical cation, $(\text{DMA})_2^{\bullet+}$, exists in solution.

Results and Discussion

Figure 1 schematically represents the formation of $(\text{DMA})_2^{\bullet+}$ initiated by pulse radiolysis of DMA. Owing to the higher con-

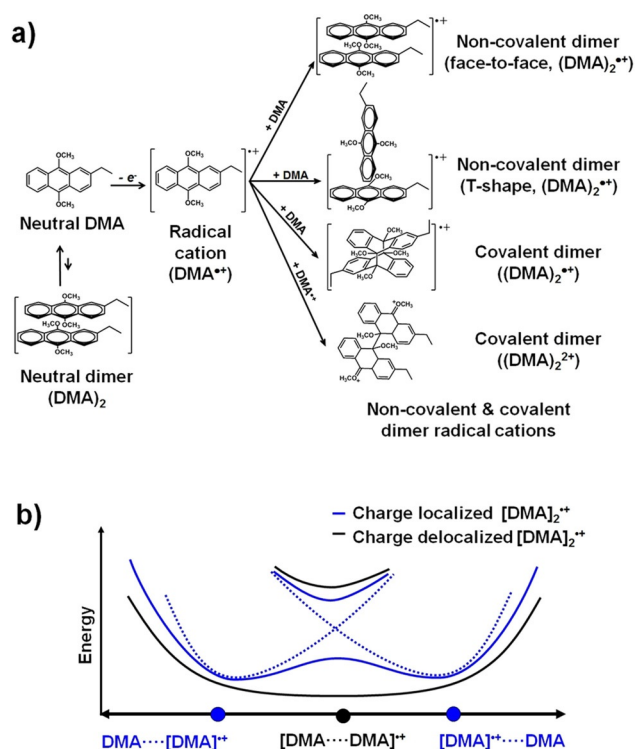


Figure 1. a) A schematic diagram of positive charge-induced dimerization of $\text{DMA}^{\bullet+}$. b) Model potential energy curves of charge-delocalized and -localized dimer radical cations. The solid and dotted lines represent the adiabatic and diabatic potential energy curves of $(\text{DMA})_2^{\bullet+}$, respectively.

centration of solvent molecules (DCE) compared to that of DMA, the electron pulse preferentially reacts with the DCE producing $\text{DCE}^{\bullet+}$ and the solvated electron (e_{sol}^-)^[40,41] followed by the generation of $\text{DMA}^{\bullet+}$ by collision between $\text{DCE}^{\bullet+}$ and DMA as shown below in Equations (1) and (2)



The generated $\text{DMA}^{\bullet+}$ may react with DMA to form $(\text{DMA})_2^{\bullet+}$ [Eq. (3)].



$(\text{DMA})_2^{\bullet+}$, formed by association between DMA and $\text{DMA}^{\bullet+}$, is most likely to be non-covalent dimer radical cations, as in the case of other aromatic dimer radical cations in solution. Face-to-face $(\text{DMA})_2^{\bullet+}$ and T-shaped $(\text{DMA})_2^{\bullet+}$ are representative structures of non-covalent $(\text{DMA})_2^{\bullet+}$, as explained later. In non-covalent $(\text{DMA})_2^{\bullet+}$, the positive charge or unpaired spin can be either delocalized over two DMA units [charge-delocalized $(\text{DMA})_2^{\bullet+}$] or localized on one of the two DMA monomers [charge-localized $(\text{DMA})_2^{\bullet+}$]. The localization or delocalization is determined by the shape of the potential energy surface for dimerization as shown in energy-coordinate diagrams in mixed-valence molecular systems (Figure 1b).^[19] We also took into account the possibility of the formation of covalent

(DMA)₂^{•+} and (DMA)₂²⁺, considering that the formation of dimeric radical cations of aromatic acetylenes has been reported^[25] and the covalent type (DMA)₂²⁺ has been produced in crystals (Figure 1 a).^[26]

Figure 2 a shows the TA spectra of DMA observed at time delays of 50 ns to 50 μs after pulse radiolysis. The absorption spectrum observed at Δt = 50 ns exhibits two strong absorption bands with the maxima located at around 430 and

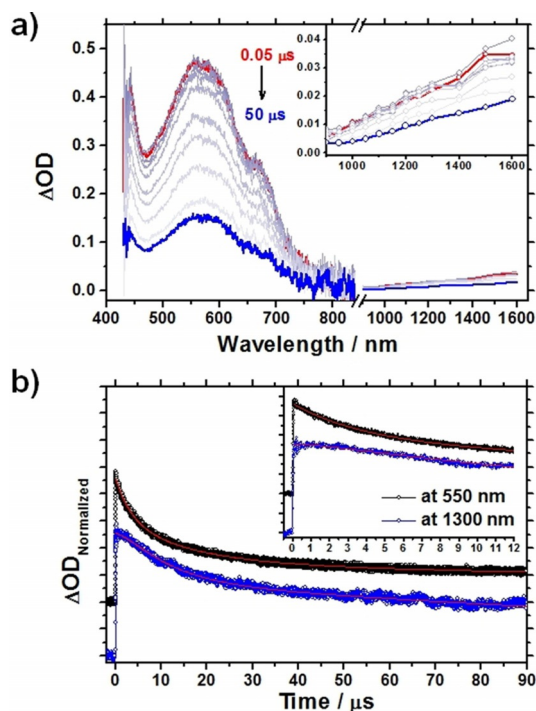


Figure 2. a) Transient absorption spectra of DMA (250 mM) in DCE at various time delays after pulse radiolysis by using an 8 ns electron pulse. The inset shows an expanded view of the near-IR transient absorption spectra. b) Decay profiles monitored at 550 nm (black) and 1300 nm (blue). Inset: Expanded view of the early time-decay profiles. The theoretical fit curve is represented by the solid red line.

560 nm and a weak absorption band in the near-IR region (900–1600 nm). The absorption signals in the visible region decrease with time without any accompanying spectral change. The time profile of the transient absorption at 550 nm includes fast and slow decay components of tens of microseconds and then a constant optical density of up to 450 μs. In addition, the time profile of transient absorption at 1300 nm includes fast-rise and slow-decay components within tens of microseconds, followed by a constant optical density. The constant optical density at long time delays observed at both 550 and 1300 nm suggests that at least one long-lived species exists in addition to DMA^{•+}. To analyze the relative concentration dependence of the long-lived species, we also measured TA spectra as a function of the DMA concentration (Figures 2 and Figures S1–S4 in the Supporting Information). As shown in Figure S4, the relative amplitude of the long-lived species concomitantly increases as the concentration of DMA increases. Furthermore, the weak absorption band in the near-IR region (900–

1600 nm), which is often used as a fingerprint for the formation of non-covalent dimer radical ions, is observed only in highly concentrated solutions (≥ 50 mM). These observations support the formation of long-lived species such as (DMA)₂^{•+}. The time constant for the rise component observed at 1300 nm is close to that of the fast decay component observed at 550 nm. Therefore, the two time profiles measured at 550 and 1300 nm were analyzed by a global fit using a triexponential function. From the global fit analysis, the time constant for the rise component observed at 1300 nm is determined to be 1.94 ± 0.03 μs. To confirm the existence of the rise component, we also fit the decay profile monitored at 1300 nm without a rise component for comparison. As shown in Figure S5 (Supporting Information), the global fit with a rise component shows a better agreement between theoretical and experimental curves. The results of visible and near-IR TA spectra clearly demonstrate that under our experimental conditions, (DMA)₂^{•+} forms with a pseudo-first order time constant of 1.94 μs by association between DMA and DMA^{•+}. Here, it is worth noting that the absorption spectra in the visible region (400–800 nm) observed at various time delays are consistent with the spectra of DMA^{•+}, as reported by Chen et al.,^[26] indicating that dimerization between DMA^{•+} and DMA does not accompany discernible changes in the TA signals in the visible region. These results suggest that the absorption spectrum of (DMA)₂^{•+} in the visible region (400–800 nm) is similar to that of DMA^{•+}. Unlike the association between DMA and DMA^{•+}, the dimerization between two DMA^{•+} to form the covalent (DMA)₂²⁺ in solution would be negligible because of the low concentration of DMA^{•+} generated by pulse radiolysis.

To address the formation of (DMA)₂^{•+} on a structural basis, we measured the steady-state Raman and TR³ spectra as a function of time after pulse radiolysis. The steady-state Raman spectrum of DMA (250 mM) in DCE, depicted in Figure 3, shows intense bands centered at 1299, 1415, 1566, and 1624 cm⁻¹. To assign the Raman bands, we calculated minimum energy structures, vibrational frequencies, and Raman activities of DMA. In DFT calculations, we found two conformers for DMA, *cis*- and *trans*-DMA, depending on the parallel and antiparallel directions of the two methoxy substituents, respectively. The relative energies and Raman activities of the two conformers are almost the same although the dipole moments of the isomers are significantly different (0.84 Debye for *trans*-DMA and 3.33 Debye for *cis*-DMA). As shown in Figure 3, the calculated Raman activities of DMA agree well with those measured in the present study. The assignment of experimental Raman bands based on the calculated vibrational normal modes and Raman activities is presented in Table 1. The strongest band at 1415 cm⁻¹ corresponds to symmetric ring stretching vibrations and the bands at 1299, 1566, and 1624 cm⁻¹ are assigned to in-plane symmetric ring breathing, symmetric ring C–C stretching, and asymmetric ring C–C stretching, respectively. DFT calculations on (DMA)₂ formed by two DMAs revealed a low dimerization energy (0.6 kcal mol⁻¹), which implies the concentration of (DMA)₂ in the current experimental conditions might be low. However, considering that the calculated Raman activities of (DMA)₂ are almost the same as those of the

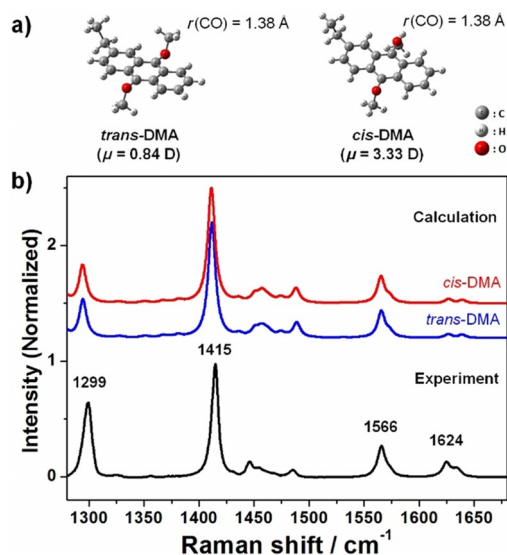


Figure 3. a) Calculated structures of *trans*- and *cis*-conformers of DMA; $r(\text{CO})$ indicates the length of the C–OCH₃ bond. b) Experimentally measured steady-state Raman spectrum of DMA (bottom black line) and Raman spectra of *cis*- and *trans*-conformers of DMA (middle) calculated by using the B3LYP/6-311 + G(d,p) theory.

DMA monomer, the steady-state Raman spectrum alone cannot provide any evidence for the absence or presence of (DMA)₂.

The TR³ spectra of transient species after pulse radiolysis of DMA were observed in the time-delay range of 30 ns to 300 μs using a 532 nm laser pulse as the Raman probe, as shown in Figure 4. It is noteworthy that the strong Raman bands of DMA are still observed as major bands in the TR³ spectra of

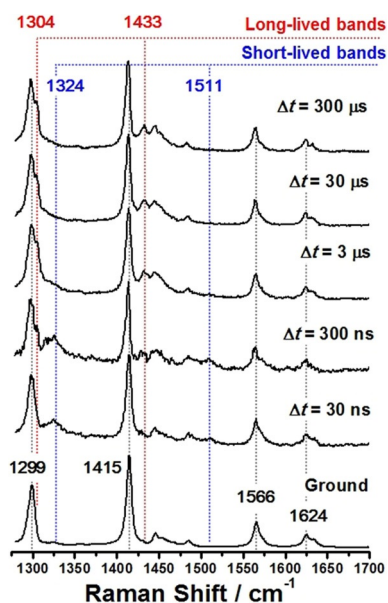


Figure 4. TR³ spectra of DMA observed at various time delays after pulse radiolysis. The peak positions corresponding to long- and short-lived bands are indicated with red and blue vertical lines, respectively. The gray-dotted vertical lines indicate the positions of intense peaks in the steady-state Raman spectrum.

the transient species, DMA^{•+} and (DMA)₂^{•+}. In addition, new Raman bands centered at 1304, 1324, 1433, and 1511 cm^{-1} were also observed (Figure 4). The Raman bands and intensities of the transient species, which are similar to those of DMA, are not due to residuals from an imperfect subtraction of the steady-state Raman spectrum. All the TR³ spectra were carefully recorded and handled to maintain identical experimental

Table 1. Experimental TR³ bands and calculated frequencies of Raman active modes (in cm^{-1}) along with their assignments for DMA in the ground state and DMA^{•+}. In the molecular structure, the numbers in red indicate the atom positions and those in blue the bond positions.

Experiments		Calculation ^[a]				Assignments ^[b]
DMA	Transient species	DMA	DMA ^{•+} (<i>cis</i>)	DMA ^{•+} (<i>trans</i>)	(DMA) ₂ ^{•+} (DT ^{•+})	
1299	1299,1304	1294	1304	1302	1296, 1310	in-plane sym., c-ring breathing
–	1324	–	1322/1325	1321/1326	1325/1330	CH ₂ wagging of ethyl group/asym. c-ring deformation
1415	1414	1411	1382	1385	1378, 1412	sym. c-ring CC stretching
–	1433	–	–	–	–	unassigned
1445	1445	1435, 1450	1440, 1450	1439, 1449	1437, 1452	asym. ring deformation
1455	1455	1455–1466	1458–1482	1456–1483	1453–1492	CH ₂ wagging
1485	1484	1488	–	–	1484	sym. CC(2,7) stretching + sym. CO stretching
–	1511	–	1509	1509	1513	sym. CC(2,7) stretching + sym. CO stretching
–	–	1531	1538	1537	1531, 1538	asym. CC(2) stretch + sym. CO bending
1566	1564	1565	1572, 1577	1571, 1576	1564, 1673	sym. CC(2) stretch + sym. CO stretching
1573	1573	1573	1485	1485	1569, 1492	asym. CC(5,6) stretching
1624	1624	1626	–	–	1585, 1627	asym. CC(1,4) stretching
1633	1633	1639	1600	1598	1603, 1639	sym. CC(1,4) stretching

[a] Calculation method: B3LYP/6-311 + G(d,p) for DMA and DMA^{•+} (scaling factor: 0.985) and B3LYP/6-31G(d) for DT^{•+} (scaling factor: 0.973). [b] Abbreviations: asym.: asymmetric; sym.: symmetric; c-ring: center-ring; CC(bond number): carbon–carbon bond (bond number).

conditions at each time delay. Each difference spectrum was obtained by subtracting the negative time-delay signal, which is identical to the steady-state Raman signal, from the spectrum at a positive time-delay using a subtraction factor large enough to avoid negative features. The retained strong peaks in the TR³ spectra, apart from the new Raman bands centered at 1304, 1324, 1433, and 1511 cm⁻¹ show a subtle but reproducible spectral shift at each band although the shift is within the bandwidth of our Raman probe. For example, the 1415 cm⁻¹ peak, which is the most intense peak in the steady-state Raman spectrum of DMA, is shifted to 1414 cm⁻¹ and the line profile of the 1299 cm⁻¹ peak is changed significantly (see Figure 4 and Figure S6 in the Supporting Information). These spectral changes suggest these intense Raman bands in the TR³ spectra originate from transient species, such as DMA⁺⁺ or (DMA)₂⁺⁺. Alternatively, the Raman bands at 1324 and 1511 cm⁻¹ disappear as the delay time increases (>3 μs), whereas the intensities of the bands at 1304 and 1433 cm⁻¹ gradually increase (0.03–300 μs). Particularly, the Raman band of 1324 cm⁻¹ is observed at Δt=1 and 3 μs, and then disappears completely at 30 μs as shown in Figure S7 (Supporting Information). This result indicates that the Raman bands at 1324 and 1511 cm⁻¹ disappear within a few microseconds, which is consistent with the result obtained from TA experiments. On the basis of the TA results that support the formation of (DMA)₂⁺⁺ by the association of DMA and DMA⁺⁺, we suggest that the Raman bands at 1324 and 1511 cm⁻¹ observed at early time delays can be attributed to DMA⁺⁺, whereas the Raman bands at 1304 and 1433 cm⁻¹ are related to (DMA)₂⁺⁺.

To assign the Raman bands of the transient species DMA⁺⁺ and (DMA)₂⁺⁺, DFT calculations were carried out and the results are depicted in Figures 5 and 6. We calculated the Raman bands of DMA⁺⁺ conformers and compared them with the Raman signal of DMA and the TR³ spectra at 30 ns and 300 μs (Figure 5). There exist *cis*- and *trans*-DMA⁺⁺, which are defined by the arrangement of the two methoxy groups, similar to DMA (Figure 5a), and it is likely that they coexist as there is no energy barrier for methoxy rotation (Figure S8, Supporting Information). The dipole moments of both conformers, *cis*- and *trans*-DMA⁺⁺, are higher than those of *cis*- and *trans*-DMA, respectively. The calculated spectra for both conformers of DMA⁺⁺ are significantly different from those of DMA and the TR³ spectra, although some transient bands in TR³ spectra agree only with the calculated DMA⁺⁺ spectra (Figure 5b). For example, the calculated spectra for both *cis*- and *trans*-DMA⁺⁺ do not include the intense band of 1414 cm⁻¹, whereas the transient band in TR³ spectra at 1511 cm⁻¹ agrees only with the calculated DMA⁺⁺ spectra (Figure 5b). On the basis of this comparison between the TR³ spectra and the calculated results, we can estimate that DMA⁺⁺ is not a major contributor to the observed TR³ spectra. Instead, the experimentally measured TR³ signals at 30 ns as well as those at 300 μs are more similar to the sum of the calculated Raman spectra of DMA and DMA⁺⁺. We speculated that the measured TR³ spectra can be predominantly attributed to (DMA)₂⁺⁺ rather than DMA⁺⁺. Considering that the TA spectra provided experimental evi-

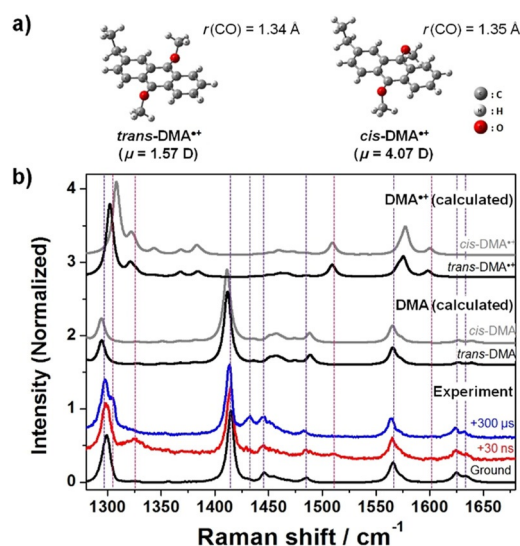


Figure 5. a) Calculated structures of *trans*- and *cis*-conformers of DMA⁺⁺. b) TR³ spectra of DMA at selected time delays after pulse radiolysis, Δt = +30 ns (bottom red) and +300 μs (bottom blue), and the Raman spectra of *cis*- and *trans*-conformers of DMA (top) calculated by using the B3LYP/6-311++G(d,p) theory. The violet- and magenta-dotted vertical lines represent the positions of the bands in agreement with the calculated Raman spectra of DMA and DMA⁺⁺, respectively.

dence for the rapid formation of (DMA)₂⁺⁺ with the pseudo-first order time constant of 1.94 μs, the existence of (DMA)₂⁺⁺ at 300 μs is understood, but the existence of (DMA)₂⁺⁺ at even at 30 ns cannot be supported by the TA results alone. At a high concentration (250 mM), the average distance between two solute molecules is not too large (<10 nm) and some of them may be much closer due to dipole-dipole interactions. The estimated collision time for diffusion-controlled association between DMA and DMA⁺⁺ upon pulse radiolysis of DMA at a high concentration is 1.2 ns according to the Stokes–Einstein relation. This result indicates the efficient and very fast route for the formation of (DMA)₂⁺⁺ is available in addition to the μs scale association observed by TA. The time resolution of near-IR TA in this work is about 30 ns, which is not fast enough to capture such a fast process. In addition to this scenario, we can also hypothesize that the weakly bounded neutral DMA dimer, (DMA)₂, can assist the rapid formation of the charge-localized (DMA)₂⁺⁺. However, as mentioned already, a quantitative analysis for (DMA)₂ from our steady-state Raman spectra is impossible due to the similarity of the Raman spectra of DMA and (DMA)₂.

To confirm that the measured TR³ spectra can be predominantly attributed to (DMA)₂⁺⁺ rather than DMA⁺⁺, various conformations of (DMA)₂⁺⁺ and their Raman activities were calculated. The results are shown in Figure 6. As depicted in Figure 1a, we consider two representative non-covalent (DMA)₂⁺⁺ [face-to-face and T-shaped (DMA)₂⁺⁺] and covalent (DMA)₂⁺⁺ (CDF⁺⁺) formed by two covalent C–C bonds between DMA and DMA⁺⁺ (Figure 6). Three face-to-face (DMA)₂⁺⁺—DF1⁺⁺, DF2⁺⁺, and DF3⁺⁺—have parallel π-stacked geometries between two anthracene moieties, whereas T-shaped DMA⁺⁺ (DT⁺⁺) has an edge-to-face geometry between two anthracene

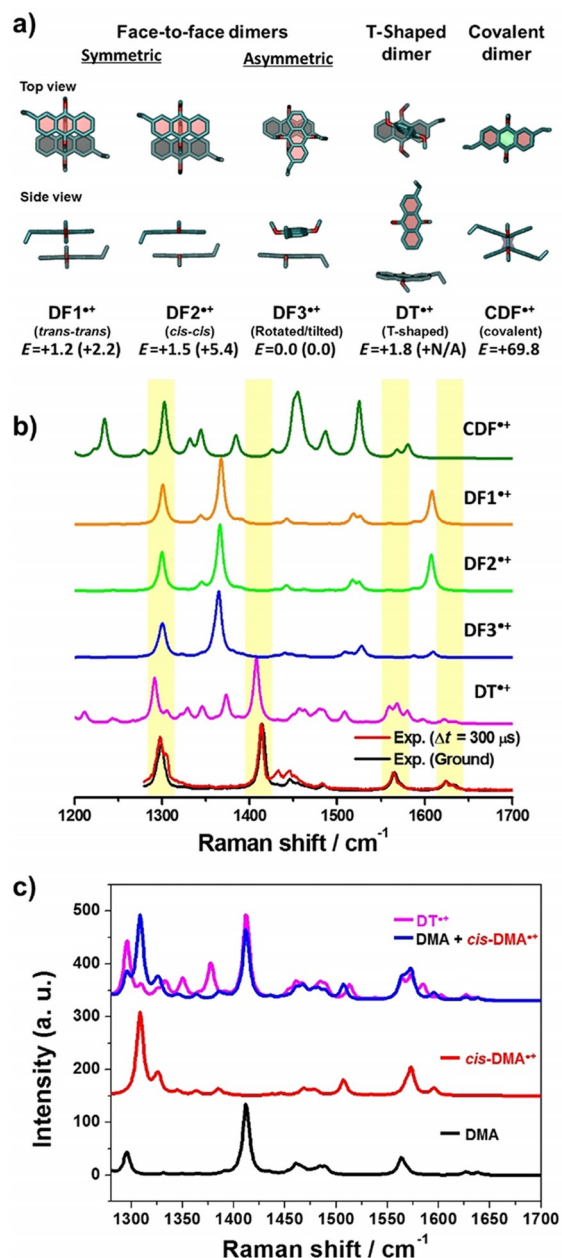


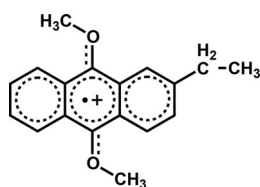
Figure 6. a) DFT-calculated $(\text{DMA})_2^{++}$ and their relative energies in kcal mol^{-1} . The values from B3LYP/6-31+G(d,p) are shown together with those from M06-2X/6-31+G(d,p) in parentheses. The red color in the tube structure format represents the oxygen atom and the hydrogen atoms are not displayed. The shaded area indicates a benzene ring. b) Calculated Raman spectra of $(\text{DMA})_2^{++}$ with the B3LYP/6-31G(d) level of theory. The yellow shaded strips indicate the positions of intense bands in both steady-state Raman and TR³ spectra. c) A comparison of the calculated Raman activities of DT⁺⁺ and the sum of calculated Raman activities of DMA and DMA⁺⁺. For the summed spectrum (blue) of DMA and DMA⁺⁺, the calculated Raman spectrum of cis-DMA⁺⁺ was used since the cationic moiety in DT⁺⁺ is in the cis-form.

moieties. Specifically, DF1⁺⁺ and DF2⁺⁺ consist of different conformations of the monomer units, *trans-trans* (DF1⁺⁺) and *cis-cis* (DF2⁺⁺), whereas the two monomer units in DF3⁺⁺ are rotated along the perpendicular axis of the anthracene plane and slightly tilted out of the exact parallel arrangement. For DT⁺⁺,

the “edge”-side monomer in the edge-to-face structure takes a *trans*-form, whereas the “face”-side monomer is in a *cis*-form with a slightly bent anthracene moiety. The calculated results demonstrate that all non-covalent $(\text{DMA})_2^{++}$ are more stable than the covalent dimer CDF⁺⁺ ($E = +69.8 \text{ kcal mol}^{-1}$) and that among the three face-to-face dimers, the asymmetric π -stacked face-to-face dimer, DF3⁺⁺, has the lowest energy, even though the relative energies of other non-covalent dimers are less than 2 kcal mol^{-1} (Figure 6a). The four C–OCH₃ bond lengths in each of DF1⁺⁺, DF2⁺⁺, and DF3⁺⁺ are almost identical (1.37 Å), whereas the C–OCH₃ bond lengths of the monomers in DT⁺⁺ are 1.33 Å in the cationic moiety and 1.38 Å in the neutral moiety, which are similar to the C–OCH₃ bond lengths in DMA⁺⁺ and DMA, respectively. Our Millikan charge calculations showed that DF1⁺⁺ and DF2⁺⁺, symmetric face-to-face dimers (C–OCH₃ bond lengths = 1.37 Å), equally share the +1 charge into two monomer units whereas the positive charge on DT⁺⁺, an edge-to-face dimer, is localized on the “face”-side monomer unit, where two C–OCH₃ bond lengths are 1.33 Å. The calculated partial charges on the two monomer units in DF3⁺⁺, an asymmetric face-to-face dimer, are +0.55 and +0.45, respectively. The comparison of the partial charge and the C–OCH₃ bond lengths of each moiety reveals a correlation between them, that is, shorter C–OCH₃ bond length in the more positively charged moiety.

The calculated vibration frequencies and Raman activities of the four dimer radical cations (DF1⁺⁺, DF2⁺⁺, DF3⁺⁺, and DT⁺⁺) by using the B3LYP/6-31G(d) method show clear differences (Figure 6b). Among the four dimer radical cations (DF1⁺⁺, DF2⁺⁺, DF3⁺⁺, and DT⁺⁺), the calculated Raman spectrum for DT⁺⁺ shows the best agreement with the TR³ spectrum. Another three face-to-face $(\text{DMA})_2^{++}$ (DF1⁺⁺, DF2⁺⁺, and DF3⁺⁺) and CDF⁺⁺ show noticeable spectral shifts and significantly different intensities with respect to the TR³ spectrum. In fact, the calculated Raman spectrum for charge-localized DT⁺⁺ is similar to the sum of each calculated spectrum of DMA and DMA⁺⁺, except the peak intensities in the range of 1300 and 1400 cm^{-1} (Figure 6c). The vibrational normal modes of DT⁺⁺ are almost the same as the sum of those of isolated monomers (DMA and DMA⁺⁺) and the deviated peaks in the range of 1300 and 1400 cm^{-1} are mainly attributed to the vibration modes of the DMA⁺⁺ moiety. Thus, the difference observed in the range of 1300 and 1400 cm^{-1} appears to be caused by the slightly more bent DMA⁺⁺ moiety in DT⁺⁺ with respect to the isolated DMA⁺⁺. Therefore, our TR³ spectra, which are similar to the sum of DFT-calculated Raman spectra of DMA and DMA⁺⁺, and results suggest that the observed TR³ may be attributed to Raman bands of charge-localized DT⁺⁺ or its analogous structures.

The TR³ bands assigned on the basis of the calculated vibrational normal modes and Raman activities of DT⁺⁺ are summarized in Table 1. The Raman bands at 1299 and 1304 cm^{-1} are attributed to the in-plane symmetric ring-breathing vibrations of DMA and DMA⁺⁺ moieties in DT⁺⁺, respectively. The Raman band at 1324 cm^{-1} corresponds to the CH₂ wagging of the ethyl substituent and asymmetric ring C–C stretching of DMA⁺⁺ moieties of DT⁺⁺. The Raman band at 1511 cm^{-1} is at-



Scheme 1. Charge delocalization in $\text{DMA}^{+\bullet}$ with two partial $\text{C}=\text{O}$ double bonds.

tributed to the symmetric ring stretching mode involving CO stretching of $\text{DMA}^{+\bullet}$ moieties of $\text{DT}^{+\bullet}$, indicating that $\text{DMA}^{+\bullet}$ has two partial $\text{C}=\text{O}$ double bonds due to charge delocalization, as shown in Scheme 1

The results obtained from the TA experiments are summarized as follows: 1) a concentration-dependent long-lived component in the visible wavelength region, 2) an absorption band in the near-IR region in high-concentration solutions (> 50 mM), and 3) a shared time constant between the decay and rise components in the visible and near-IR regions, respectively. Furthermore, our TR^3 spectra show the best agreement with the calculated Raman spectrum for $\text{DT}^{+\bullet}$, which is similar to the sum of the two Raman spectra of DMA and $\text{DMA}^{+\bullet}$. A similar spectral behavior was observed for the 4,4'-dinitrotolane radical anion, which exhibited overlapping Raman peaks originating from its neutral and monoanionic species.^[21,22] Thus, we suggest that $(\text{DMA})_2^{+\bullet}$ formed by the association between DMA and $\text{DMA}^{+\bullet}$ is likely to be in the charge-localized state, similar to the 4,4'-dinitrotolane radical anion.

DFT-calculated binding energy of $(\text{DMA})_2^{+\bullet}$ [$3.4 \text{ kcal mol}^{-1}$ for B3LYP/6-31+G(d,p)] is larger than that of $(\text{DMA})_2$ [$0.6 \text{ kcal mol}^{-1}$ for B3LYP/6-31+G(d,p)]. This means that the positive charge-induced association between $\text{DMA}^{+\bullet}$ and DMA is more favorable than the dimerization between two DMAs driven by van der Waals interactions. Here, we consider the driving force for the formation of $(\text{DMA})_2^{+\bullet}$ by the association between DMA and $\text{DMA}^{+\bullet}$. Figure 7a shows a schematic diagram of positive charge-induced dimerization as well as the dimerization of two neutral monomers. When a $\text{DMA}^{+\bullet}$ is generated by pulse radiolysis, DMA and $\text{DMA}^{+\bullet}$ are attracted to each other by enhanced Coulomb forces induced by the permanent positive charge of $\text{DMA}^{+\bullet}$, compared with the attraction between two neutral DMAs. To find the minimum energy route for dimerization between DMA and $\text{DMA}^{+\bullet}$, we carried out partial geometry optimizations at a fixed distance between C_9 atoms in DMA and $\text{DMA}^{+\bullet}$ using the B3LYP/6-31G(d) method and also conducted the equivalent calculations on the dimerization of two DMAs to compare the effect of the positive charge (Figure 7b). $\text{DF3}^{+\bullet}$ was used as the starting geometry of the partial geometry optimization. The calculated energy profiles for $(\text{DMA})_2^{+\bullet}$ and $(\text{DMA})_2$ are shown in Figure 7b and the representative minimum energy structures of $(\text{DMA})_2^{+\bullet}$ (I, II, and III) are shown as well. Upon increasing the C_9 - C_9 distance, the optimized geometries of $(\text{DMA})_2^{+\bullet}$ underwent a significant change—symmetric parallel face-to-face (I) \rightarrow rotated asymmetric face-to-face (II) \rightarrow edge-to-face configuration (III). Notably, the potential energy profile of $(\text{DMA})_2^{+\bullet}$ is quite flat in the range of 3 to 6 Å, suggesting that structural changes are relatively easy and a variety of asymmetric dimeric structures can coexist in solution. In contrast, the energy profile of $(\text{DMA})_2$ is repulsive without local minima within the calculated range of 1 to 7.5 Å. In fact, structure III in Figure 7b is different from

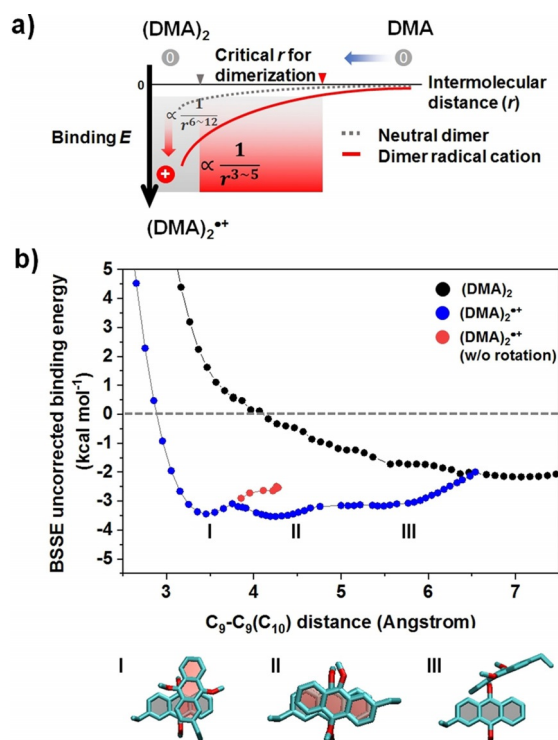


Figure 7. A schematic diagram of the positive charge-induced dimerization in DMA and the relaxed potential energy surface along the monomer-monomer distance. a) A schematic potential energy curve corresponding to the dimerization of two DMAs in $(\text{DMA})_2$ and charge-induced dimerization in $(\text{DMA})_2^{+\bullet}$. The dotted-gray and solid-red curves indicate the schematic energy curves of $(\text{DMA})_2$ and $(\text{DMA})_2^{+\bullet}$, respectively. b) Potential energy curves (filled black and blue circles, respectively) of $(\text{DMA})_2$ and $(\text{DMA})_2^{+\bullet}$ in 1,2-dichloroethane optimized at different C_9 - $\text{C}_9(\text{C}_{10})$ distances using B3LYP/6-31G(d) method. The filled red curve indicates the continued potential energy curve without rotation of one DMA moiety starting from $\text{DF2}^{+\bullet}$ structure. Bottom: Three representative structures of $(\text{DMA})_2^{+\bullet}$ denoted in the potential energy curve.

that of $\text{DT}^{+\bullet}$. This might be due to the effect of the starting geometry, $\text{DF3}^{+\bullet}$, for the geometry optimization at fixed C_9 - C_9 bond length. The relative energy of structure III is similar to those of the $(\text{DMA})_2^{+\bullet}$ structures shown in Figure 6a, which were obtained by full-geometry optimization. Thus, we can conjecture that various asymmetric edge-to-face dimers, such as structure III in Figure 7b and $\text{DT}^{+\bullet}$, are available on the conformational landscape of the dimer radical cation instead of only a few major structures. In other words, the charge-localized dimer radical cations, such as $\text{DT}^{+\bullet}$ and III depicted in Figure 7b, may be populated in a context of dynamical equilibrium even at room temperature owing to continuous interconversion between charge-localized and delocalized structures, considering the relatively low dimerization energy of $(\text{DMA})_2^{+\bullet}$ compared to the dimerization energy of a benzene dimer radical cation ($\approx 20 \text{ kcal mol}^{-1}$).^[31]

Describing the non-covalent interactions and predicting charge (or spin) localization/delocalization are still some of the most challenging issues in DFT.^[42] In practice, some studies by using the B3LYP method, which is the most widely used DFT method for a wide range of systems, failed to yield correct dissociation energies for simple radical homodimer ions due to a

self-interaction error.^[43–45] In contrast, Fujitsuka et al. showed that B3LYP calculations accurately predicted the correlation between averaged transannular distance and the position of the charge resonance band for multiple-layered cyclopropanes.^[6] To evaluate the reliability of the calculated results, we analyzed the vibration frequencies, Raman activities, and conformations of $(\text{DMA})_2^{*+}$ with different levels of calculations—three different DFT methods (B3LYP, CAM-B3LYP, and M06-2X) and different levels of basis sets [6-31G and 6-31+G(d,p)]. The calculation results are summarized in Table S1 (Supporting Information). It can be seen in the table that DF3^{*+} is the most stable structure in all the calculations, although the relative energies of other structures are substantially changed. In particular, the relative energy of DT^{*+} is reduced by using the larger 6-31+G(d,p) basis set or the CAM-B3LYP method (+1.8 and 0.4 kcal mol⁻¹), whereas M06-2X calculations with either 6-31G(d) or 6-31+G(d,p) failed to find a DT^{*+} -like minimum energy structure; in addition, the inter-monomer distance for $(\text{DMA})_2^{*+}$, the Raman activities, and near-IR vertical transition energies of $(\text{DMA})_2^{*+}$ strongly rely on the DFT method that is used. In particular, compared to the B3LYP method, the M06-2X method exhibited excessively large dimerization energies for $(\text{DMA})_2$ and $(\text{DMA})_2^{*+}$ [14.3 kcal mol⁻¹ for $(\text{DMA})_2$ and 20.3 kcal mol⁻¹ for $(\text{DMA})_2^{*+}$] and a narrower vertical excitation energy distribution in the visible wavelength range than in the visible TA signal (Figure S9, Supporting Information). Therefore, among the DFT methods tested in this study, the B3LYP method supported our experimental findings relatively well and, thus, was mainly used for interpretation of our experimental results.

Conclusions

In this study, we found spectroscopic evidence for charge-localized DMA dimer radical cations by using TA and TR³ spectroscopic methods coupled with pulse radiolysis. The formation of DMA^{*+} and $(\text{DMA})_2^{*+}$ was observed by monitoring the Vis and near-IR TA spectra. The concentration-dependent long-lived component in the Vis-TA and the rise component in near-IR TA spectra demonstrate that the generated DMA^{*+} is stabilized by the association with neutral DMA. The TR³ spectra obtained after pulse radiolysis of DMA revealed that the most intense bands in the steady-state Raman spectrum of DMA are also the major dominant bands in the TR³ spectra observed at all time delays from 30 ns to 300 μs without significant changes of the positions and relative intensities except for the small transient bands. DFT calculations for $(\text{DMA})_2^{*+}$ revealed that an asymmetric π -stacked face-to-face $(\text{DMA})_2^{*+}$, DF3^{*+} , is more stable than edge-to-face T-shaped $(\text{DMA})_2^{*+}$, DT^{*+} , whereas the observed TR³ spectra agree better with the calculated Raman spectrum of DT^{*+} , which is similar to the sum of the Raman spectra of DMA and DMA^{*+} . Through a comparison with DFT calculation results, we suggest that the intense bands in TR³ spectra are most likely attributable to Raman bands of charge localized dimer radical cations, such as DT^{*+} , and that the charge-localized $(\text{DMA})_2^{*+}$ form efficiently in less than 30 ns. In addition, the DFT-calculated potential energy curve for the association of DMA and DMA^{*+} shows that the en-

hanced Coulomb interactions induced by the permanent charge of DMA^{*+} could help the association between DMA and DMA^{*+} and the stabilization of charge-localized dimer radical cations in the context of dynamic equilibrium.

Experimental Section

General: DMA was purchased from Sigma Aldrich and was used without further purification. The samples were prepared by dissolving DMA in DCE (Tokyo Chemical Industry Co., Ltd), resulting in solution concentrations of 0.5 to 500 mM. Pulse radiolysis was triggered by using an electron pulse (27 MeV, 11 A, 8 ns, 0.8 kGy per pulse) generated by a linear accelerator at Osaka University. TR³ measurements after pulse radiolysis were carried out by passing the sample solution through a quartz capillary tube at a sufficient rate to ensure that each pair of electron and laser pulses encountered a fresh sample volume. The sample was exposed to a 532 nm laser pulse generated by the second harmonic output from a nanosecond Q-switched Nd:YAG laser (5 ns FWHM, Brilliant, Quantel; Les Ulis, France). The Raman probe was synchronized with the electron pulse. The TR³ spectra were collected using a polychromator (Acton, SP2500i; Trenton, NJ, USA) equipped with a charge-coupled device camera (Princeton Instruments, PI-MAX3; Trenton, NJ, USA).

Computational methods: DFT calculations were conducted to find the minimum-energy structures of DMA, DMA^{*+} , and $(\text{DMA})_2^{*+}$ by using the B3LYP,^[46,47] CAM-B3LYP,^[48] and M06-2X^[49] methods. The solvation effects of DCE were included by using the polarized continuum model (IEF-PCM). The vibration frequencies and Raman activities of DMA, DMA^{*+} , and $(\text{DMA})_2^{*+}$ in DCE were calculated to assign the experimental Raman spectra. For the calculated vibration frequencies of DMA and DMA^{*+} , we applied the appropriate scaling factors [0.985 for B3LYP/6-311++G(d,p) and 0.973 for B3LYP/6-31G(d)]. All the calculations were performed using the Gaussian 09 suite of programs.^[50]

Acknowledgements

We thank the members of the Research Laboratory for Quantum Beam Science of SANKEN, Osaka University for running the linear accelerator. This work was partly supported by a Grant-in-Aid for Scientific Research (Projects 25220806 and others) from the Ministry of Education, Culture, Sports, Science and Technology (MEXT) of Japanese Government, and by IBS-R004, Korea.

Conflict of interest

The authors declare no conflict of interest.

Keywords: charge localization · pulse radiolysis · radical ions · resonance Raman · time-resolved spectroscopy

- [1] J. Hankache, O. S. Wenger, *Chem. Rev.* **2011**, *111*, 5138.
- [2] A. Heckmann, C. Lambert, *Angew. Chem. Int. Ed.* **2012**, *51*, 326; *Angew. Chem.* **2012**, *124*, 334.
- [3] A. Kira, M. Imamura, *J. Phys. Chem.* **1979**, *83*, 2267.
- [4] H. Ohkita, T. Fushimi, K. Atsumi, Y. Fujita, S. Ito, M. Yamamoto, *Chem. Phys. Lett.* **2003**, *374*, 137.

- [5] A. Tsuchida, M. Yamamoto, *J. Photochem. Photobiol. A* **1992**, *65*, 53.
- [6] M. Fujitsuka, S. Tojo, M. Shibahara, M. Watanabe, T. Shinmyozu, T. Majima, *J. Phys. Chem. A* **2011**, *115*, 741.
- [7] A. Błoch-Mechkour, T. Bally, *Phys. Chem. Chem. Phys.* **2015**, *17*, 10624.
- [8] M. Hara, S. Tojo, K. Kawai, T. Majima, *Phys. Chem. Chem. Phys.* **2004**, *6*, 3215.
- [9] M. Fujitsuka, S. Samori, M. Hara, S. Tojo, S. Yamashiro, T. Shinmyozu, T. Majima, *J. Phys. Chem. A* **2005**, *109*, 3531.
- [10] K. Kawai, H. Yoshida, T. Takada, S. Tojo, T. Majima, *J. Phys. Chem. B* **2004**, *108*, 13547.
- [11] K. Kawai, H. Yoshida, A. Sugimoto, M. Fujitsuka, T. Majima, *J. Am. Chem. Soc.* **2005**, *127*, 13232.
- [12] K. Kawai, K. Miyamoto, S. Tojo, T. Majima, *J. Am. Chem. Soc.* **2003**, *125*, 912.
- [13] T. N. Das, *J. Phys. Chem. A* **2009**, *113*, 6489.
- [14] M. Yamamoto, Y. Tsujii, A. Tsuchida, *Chem. Phys. Lett.* **1989**, *154*, 559.
- [15] A. Kira, S. Arai, M. Imamura, *J. Phys. Chem.* **1972**, *76*, 1119.
- [16] J. K. Kochi, R. Rathore, P. L. Maguères, *J. Org. Chem.* **2000**, *65*, 6826.
- [17] M. Fujitsuka, S. Tojo, T. Shinmyozu, T. Majima, *Chem. Commun.* **2009**, 1553.
- [18] A. Tsuchida, H. Takamura, M. Yamamoto, *Chem. Phys. Lett.* **1992**, *198*, 193.
- [19] K. D. Demadis, C. M. Hartshorn, T. J. Meyer, *Chem. Rev.* **2001**, *101*, 2655.
- [20] T. Mani, D. C. Grills, M. D. Newton, J. R. Miller, *J. Am. Chem. Soc.* **2015**, *137*, 10979.
- [21] R. M. Hoekstra, J. P. Telo, Q. Wu, R. M. Stephenson, S. F. Nelsen, J. I. Zink, *J. Am. Chem. Soc.* **2010**, *132*, 8825.
- [22] R. M. Hoekstra, Y.-T. Chen, M. D. Kiesz, J. P. Telo, R. M. Stephenson, S. F. Nelsen, J. I. Zink, *Can. J. Chem.* **2014**, *92*, 940.
- [23] M. Kaupp, M. Renz, M. Parthey, M. Stolte, F. Würthner, C. Lambert, *Phys. Chem. Chem. Phys.* **2011**, *13*, 16973.
- [24] W. Jiang, C. Xiao, L. Hao, Z. Wang, H. Ceymann, C. Lambert, S. Di Motta, F. Negri, *Chem. Eur. J.* **2012**, *18*, 6764.
- [25] T. Majima, S. Tojo, S. Takamuku, *J. Phys. Chem. A* **1997**, *101*, 1048.
- [26] X. Chen, X. Wang, Z. Zhou, Y. Li, Y. Sui, J. Ma, X. Wang, P. P. Power, *Angew. Chem. Int. Ed.* **2013**, *52*, 589; *Angew. Chem.* **2013**, *125*, 617.
- [27] D.-L. Sun, S. V. Rosokha, S. V. Lindeman, J. K. Kochi, *J. Am. Chem. Soc.* **2003**, *125*, 15950.
- [28] S. V. Lindeman, S. V. Rosokha, D. Sun, J. K. Kochi, *J. Am. Chem. Soc.* **2002**, *124*, 843.
- [29] T. Majima, S. Tojo, A. Ishida, S. Takamuku, *J. Phys. Chem.* **1996**, *100*, 13615.
- [30] P. A. Pieniazek, A. I. Krylov, S. E. Bradforth, *J. Chem. Phys.* **2007**, *127*, 044317.
- [31] P. A. Pieniazek, S. E. Bradforth, A. I. Krylov, *J. Chem. Phys.* **2008**, *129*, 074104.
- [32] J. R. Grover, E. A. Walters, E. T. Hui, *J. Phys. Chem.* **1987**, *91*, 3233.
- [33] Y. Inokuchi, Y. Naitoh, K. Ohashi, K. Saitow, K. Yoshihara, N. Nishi, *Chem. Phys. Lett.* **1997**, *269*, 298.
- [34] S. A. Milosevich, K. Saichek, L. Hinchey, W. B. England, P. Kovacic, *J. Am. Chem. Soc.* **1983**, *105*, 1088.
- [35] K. Hiraoka, S. Fujimaki, K. Argua, *J. Chem. Phys.* **1991**, *95*, 8413.
- [36] S. P. Platt, I. K. Attah, S. Aziz, M. S. El-Shall, *J. Chem. Phys.* **2015**, *142*, 191102.
- [37] M. J. Rusyniak, Y. M. Ibrahim, D. L. Wright, S. N. Khanna, M. S. El-Shall, *J. Am. Chem. Soc.* **2003**, *125*, 12001.
- [38] I. K. Attah, A.-R. Soliman, S. P. Platt, M. Meot-Ner (Mautner), S. G. Aziz, M. S. El-Shall, *Phys. Chem. Chem. Phys.* **2017**, *19*, 6422.
- [39] H. Bouas-Laurent, A. Castellan, J.-P. Desvergne, R. Lapouyade, *Chem. Soc. Rev.* **2000**, *29*, 43.
- [40] T. Sumiyoshi, N. Sugita, K. Watanabe, M. Katayama, *Bull. Chem. Soc. Jpn.* **1988**, *61*, 3055.
- [41] H. Mohan, P. N. Moorthy, *J. Chem. Soc. Perkin Trans. 2* **1990**, 277.
- [42] A. J. Cohen, P. Mori-Sánchez, W. Yang, *Chem. Rev.* **2012**, *112*, 289.
- [43] T. Bally, G. N. Sastry, *J. Phys. Chem. A* **1997**, *101*, 7923.
- [44] Y. Zhang, W. Yang, *J. Chem. Phys.* **1998**, *109*, 2604.
- [45] J. Gräfenstein, E. Kraka, D. Cremer, *J. Chem. Phys.* **2004**, *120*, 524.
- [46] C. Lee, W. Yang, R. G. Parr, *Phys. Rev. B* **1988**, *37*, 785.
- [47] A. D. Becke, *J. Chem. Phys.* **1993**, *98*, 5648.
- [48] T. Yanai, D. P. Tew, N. C. Handy, *Chem. Phys. Lett.* **2004**, *393*, 51.
- [49] Y. Zhao, D. G. Truhlar, *Theor. Chem. Acc.* **2008**, *120*, 215.
- [50] Gaussian 09 (Revision A.02), M. J. Frisch, G. W. Trucks, H. B. Schlegel, G. E. Scuseria, M. A. Robb, J. R. Cheeseman, G. Scalmani, V. Barone, B. Mennucci, G. A. Petersson, H. Nakatsuji, M. Caricato, X. Li, H. P. Hratchian, A. F. Izmaylov, J. Bloino, G. Zheng, J. L. Sonnenberg, M. Hada, M. Ehara, K. Toyota, R. Fukuda, J. Hasegawa, M. Ishida, T. Nakajima, Y. Honda, O. Kitao, H. Nakai, T. Vreven, J. A. Montgomery, Jr., J. E. Peralta, F. Ogliaro, M. Bearpark, J. J. Heyd, E. Brothers, K. N. Kudin, V. N. Staroverov, R. Kobayashi, J. Normand, K. Raghavachari, A. Rendell, J. C. Burant, S. S. Iyengar, J. Tomasi, M. Cossi, N. Rega, J. M. Millam, M. Klene, J. E. Knox, J. B. Cross, V. Bakken, C. Adamo, J. Jaramillo, R. Gomperts, R. E. Stratmann, O. Yazyev, A. J. Austin, R. Cammi, C. Pomelli, J. W. Ochterski, R. L. Martin, K. Morokuma, V. G. Zakrzewski, G. A. Voth, P. Salvador, J. J. Dannenberg, S. Dapprich, A. D. Daniels, O. Farkas, J. B. Foresman, J. V. Ortiz, J. Cioslowski, D. J. Fox, Gaussian, Inc., Wallingford CT, **2009**.

Manuscript received: January 12, 2019
Version of record online: March 20, 2019